IJBBE International Journal of Biophotonics & Biomedical Engineering Vol. 3, No. 2, Summer-Fall, 2023

Research Article

Fluence and wavelength optimization of pulsed laser in photothermal therapy

N. Amjadi and R. Malekfar *

Atomic and Molecular Group, Physics Department, Faculty of Basic Sciences,
Tarbiat Modares University, Tehran P.O. Box 14115-175, I.R. Iran

*** Corresponding Author Email: Malekfar@Modares.ac.ir**

DOI: 10.30495/ijbbe.2024.2003311.1038

ABSTRACT

Received: Dec. 8, 2023, Revised: Jan. 2, 2024, Accepted: Jan. 10, 2024, Available Online: Feb. 5, 2024

The ability of Plasmonic nanoparticles (PNPs) to efficiently convert absorbed light energy into localized heat has made them a popular choice for photothermal medical applications. However, during the photothermal process, the diffusion of localized heat can lead to temperature management challenges. To address this issue, researchers have developed a new generation of PNPs incorporating optical phase transition materials, allowing for tunable photothermal responses without altering the geometry. This tunability is achieved through rapid changes in optical and thermal properties during phase transitions. In this study, we conducted a numerical analysis on the photothermal response of a VO2@Au smart nanoshell in both tumor and healthy liver tissue under irradiation with a nanosecond (5 ns) pulsed laser. To obtain the temperature profile, we solved a coupling problem between electromagnetism and thermodynamics.

KEYWORDS

Pulsed laser; Plasmonic nanoparticles; photothermal; medical applications; VO2@Au; nanoshell.

I. INTRODUCTION

In light of the high mortality rate associated with cancer, researchers are striving to develop faster and more accurate diagnostic methods and effective treatments [1-3]. Although conventional treatments such as chemotherapy, radiotherapy, and surgery are effective and widely used in clinical settings, patients are at an increased risk of treatment failure or adverse post-treatment events [4, 5]. Photothermal therapy (PTT) is among the latest cancer treatments that utilize the photothermal effect and photothermal agent (PTA) to convert absorbed light energy into heat and induce thermal burns in the tumor. PTT is highly valued for its simplicity, short treatment time, and rapid recovery [6,7]. Most importantly, PTT is an extremely effective and non-invasive treatment that aims to treat several types of cancer without causing damage to healthy tissue [8-10].

Photothermal therapy works by exposing biological tissue to laser energy, which is absorbed to varying degrees [11-13]. In the case of visible light lasers, the high light absorption coefficient of biological tissue leads to a significant amount of energy absorption, resulting in a sharp temperature rise.

Furthermore, heat conduction causes the temperature of the surrounding tissue to increase excessively [14, 15].

In contrast, when using an infrared laser, the light absorption coefficient of biological tissue is low. As a result, the increase in tissue temperature is small due to the low absorption of light energy. Therefore, photothermal agents are introduced into the tumor tissue to raise the temperature to the desired range. Photothermal agents are composed of many different materials, of which gold nanoparticles (AuNPs) are widely used because they are nontoxic to the human body [14, 15]. Moreover, to solve the problem of excessive heat transfer by conduction of heat to surrounding tissues, tunable VO2 nanoparticles can be used [16].

Understanding the relationship between temperature and biological tissue death is crucial in photothermal therapy, as an increase in temperature is known to induce tumor death [17,18]. In this study, we conducted numerical investigations on the photothermal response of a VO2@Au smart nanoshell in both tumor tissue and healthy liver tissue under irradiation with a nanosecond pulsed laser (5 ns). We solved the coupling problem of electromagnetism and thermodynamics to obtain the temperature profile. Our calculations were performed at two wavelengths, 736 and 866 nm, which correspond to the two peaks of the absorption spectrum of the nanoshell during the phase transition of the VO2 core.

After analyzing the results of step 1, we were able to identify the optimal size of the nanoshell and the incident laser pulse wavelength by calculating the difference in the absorption cross-section for the semiconductor and metallic phases of the VO2 core. Our calculations revealed that the maximum difference in the infrared absorption spectrum was achieved at two wavelengths of 736 and 866 nm, with a nanoshell radius of 30@37 nm.

Moving on to step 2, we determined that VO2 was at the phase transition threshold at 736 and 866 nm for fluences of 2.42 and 1.22 mJ/cm2, respectively. Furthermore, at these wavelengths and with minimum fluences of 3.055 and 1.643 mJ/cm2, respectively, VO2 reached a critical temperature of 68°C and underwent a phase transition.

II. METHODS

This section provides an overview of the physical model and numerical method used to simulate the interaction between the pulsed laser and the VO2@Au smart nanoshell (Figure 1). Initially, the finite element method was utilized to simulate the absorption cross-section of the VO2@Au nanoshell to optimize the size of the nanoshell and the wavelength of the incident laser. Following this, the amplified field was calculated once the size and wavelength of the incident laser were optimized.

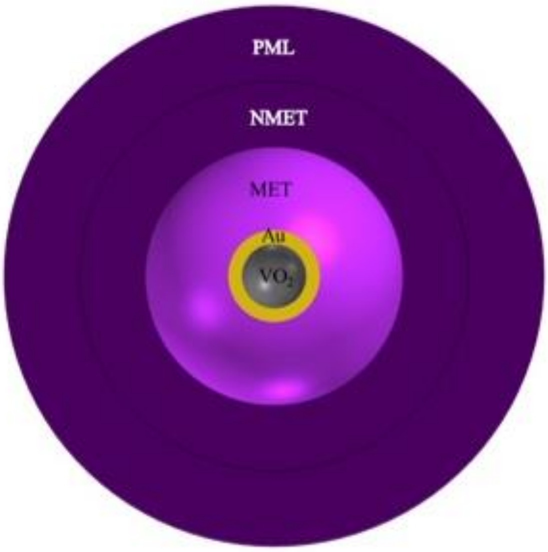

Fig. **1** depicts a schematic representation of VO2@Au embedded in liver tissue. The schematic indicates the diameter (D) of VO2, the thickness of the Au shell, the thickness of the perfect match layer (PML), and the radius of healthy and metastatic liver tissues, which are 60, 7, 70, 60, and 77.5 nm, respectively.

A. *Calculation of the absorption cross-section*

Under the assumption that the materials are homogeneous, isotropic, and nonmagnetic and that their optical properties are determined by the local dielectric function, the problem of electromagnetism and the Helmholtz equation were resolved. The Helmholtz equation is expressed by the following equation:

$$\nabla \times \mu_r^{-1}\left(\nabla \times \mathbf{E}\right) - k_0^2\left(\varepsilon_r - \frac{j\sigma}{\omega\varepsilon_0}\right)\mathbf{E} = 0 \qquad (1)$$

The relative and vacuum permittivity (εr and ε0), relative permeability (μr), conductivity (σ), and wavenumber (k0) were all considered in solving the Helmholtz equation.

The results of solving the Helmholtz equation were used to calculate the absorption cross-section (eq.2) and the scattering cross-section (eq.3) for both the medium and the nanoshell [19], using the following equations:

$$C_a = \frac{2}{c\varepsilon_0 n_\omega \left|\mathbf{E}_i\right|^2}\iiint \frac{1}{2}\mathrm{Re}\left(\mathbf{J}.\mathbf{E}^*\right)dV \qquad (2)$$

$$C_s = \frac{2}{c\varepsilon_0 n_\omega \left|\mathbf{E}_i\right|^2}\iint \frac{1}{2}\left[\mathbf{n}.\mathrm{Re}\left(\mathbf{E}_s \times \mathbf{H}_s^*\right)dS\right] \qquad (3)$$

The equations for calculating the absorption and scattering cross-sections involve the speed of light in the vacuum (c) and the refractive index of liver tissue (nω). Additionally, the current density (J) is calculated based on the product of the conductivity (σ) and electric field (E), where E is the sum of the incident and scattered electric fields (Ei + Es), and Hs represents the scattered magnetic field.

To determine the absorption and scattering cross-sections, the wavelength-dependent dielectric coefficient of gold was obtained from Johnson et al's work [20]. Meanwhile, the dielectric coefficient of the VO2 core was calculated using the Maxwell-Garnett theory [21].

B. *Calculation of the Threshold Fluence*

The subsequent step involves analyzing heat diffusion and determining the optimal fluence required for the process. In this calculation, VO2@Au is considered a heat source that absorbs electromagnetic radiation. The heat diffusion equation is solved for the isotropic system consisting of the nanoshell and its surrounding environment to determine the optimal fluence necessary for inducing a phase transition in VO2. The heat diffusion equation is expressed as:

$$\rho c_p \frac{\partial T}{\partial t} + \nabla.q = Q \qquad (4)$$

In the heat diffusion equation, the term q = −k∇T represents the heat flux, where k is the thermal conductivity and T(r,t) is the temperature as a function of both coordinate r and time t. The heat source Q = Qrh × f(τw) generated by the pulsed laser absorbed in the nanoshell is included in this equation, where Qrh refers to the resistive losses, ρ is the mass density, and cp is the heat capacity. Additionally, f(τw) is a Gaussian profile that denotes the time dependence of the pulsed laser, while τw represents the laser width [22].

$$f\left(\tau_w\right) = \frac{1}{b\sqrt{2\pi}}e^{-(t-5b)^2/2b^2}$$

$$b = \frac{\tau_w}{2\sqrt{2\ln(2)}} \qquad (5)$$

Table **1** List of the thermodynamic properties of VO_2 and Au.

materials **Properties**	Au[22]	VO_2
Density (kg/m^3)	19300	4590+30* *f*(T) [23]
Heat capacity (J/kg.K)	129	690 [24]
Thermal conductivity (W/m.K)	318	3+3.5 *f(T)* [24]
Thermal expansion coefficient (1/K)	14.2×10^{-6}	α_{VO2} [25]

THE OPTICAL PROPERTIES OF BOTH HEALTHY AND METASTASIZED LIVER TISSUE

The refractive index is an optical parameter that plays a crucial role in describing the interactions between matter and light. In tissue, when the laser beam comprises a coherent component that corresponds to the "average" electromagnetic field, its intensity decreases as it penetrates deeper into the tissue. Moreover, there is a scattering component that is associated with the local fluctuations of the electromagnetic field around its average value [26].

Table **2** displays the refractive index of both healthy and metastasized liver tissue [26].

Wavelength Tissue	The real part of the refractive index				
	450 nm	532 nm	632.8 nm	964 nm	1551 nm
Metastasis	1.365	1.359	1.355	1.349	1.343
Healthy	1.388	1.379	1.376	1.368	1.361
Wavelength Tissue	The imaginary part of the refractive index $\times 10^4$				
	450 nm	532 nm	632.8 nm	964 nm	1551 nm
Metastasis	61	59	57	46	38
Healthy	52	51	49	43	39

Table **3** presents the thermodynamic parameters of both healthy and metastatic liver tissue, as per reference [27].

Properties Tissue	Density (kg/m^3)	Heat capacity (J/kg.K)	Thermal conductivity (W/m.K)
Healthy	1080	3455	0.515
Metastasis	1045	3760	0.6

III. RESULTS

A. *Electromagnetic Wave Propagation*

The initial step involved solving the electromagnetic problem to calculate the absorption cross-section of VO2@Au in both the semiconductor and metallic phases of the VO2 core. By calculating the difference between the absorption cross-sections of the two phases, the optimal size and wavelength of the incident laser were determined. Figure 1 provides a general schematic of the proposed nanoshell and its surrounding environment.

As the core size increases, a redshift in the absorption cross-section is observed, while an increase in the thickness results in a blue shift [28]. Our calculations were limited to nanoparticles that could be synthesized within a specific size range. In this structure, gold has a lower work function (4.8 eV) than VO2 (5.4 eV), leading to the transfer of electrons from gold to VO2. In addition, the Fermi level of gold is close to the VO2 conduction band in the semiconductor phase, ensuring core-shell stability [29, 30]. The near-infrared (NIR) absorption wavelength was chosen for imaging deep samples, considering the balance between light scattering and absorption [31]. This balance is due to the fact that NIR light has lower absorption and scattering compared to visible light, making it more efficient at penetrating biological tissue [32].

The absorption cross-section was calculated for two different thicknesses of both semiconductor and metallic phases, where the core diameter of VO2 was kept constant at 60 nm. To achieve high discrimination as per MIT (metal-insulator transition), we examined the difference in the absorption cross-sections of the semiconductor and metallic phases of the VO2 core (Figure 2). The optical properties of VO2, such as the optical coefficient (refractive index "n" and extinction coefficient "k"), lattice structure, lattice parameters, and conductivity, change before and after MIT, leading to alterations in transmission, reflection, and absorption [33].

The most significant difference in absorption cross-section between the semiconductor and metallic phases in the NIR region was observed for a radius of 30@37 nm at 736 and 866 nm (indicated by the dark red dashed line in Figure 2). As per the calculations, the metallic and semiconductor phases exhibited higher absorption cross-sections at 736 and 866 nm, respectively, as indicated by the dark red dashed line in Figure 2. Based on these differences in absorption cross-section, the size and wavelength of the incident laser were selected for the simulation.

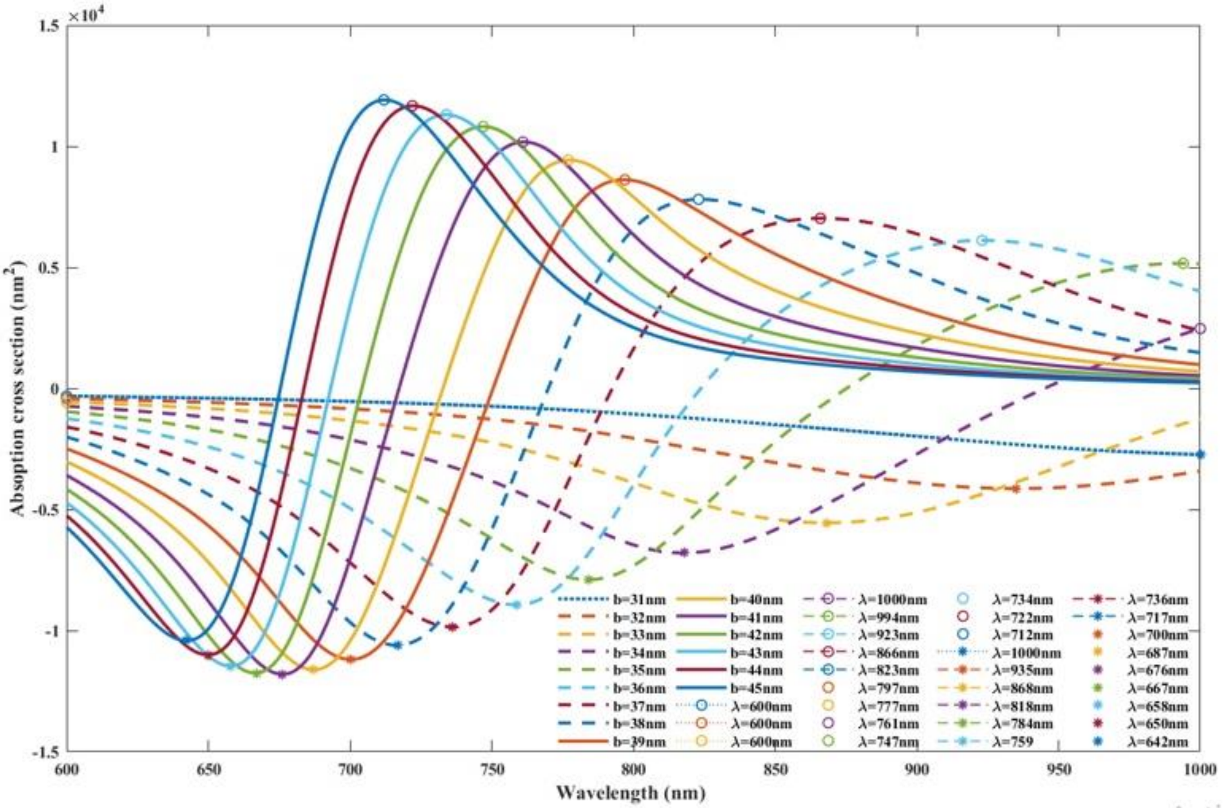

Fig. **2** illustrates the absorption cross-section for various shell thicknesses in the phase difference (CaS - CaM).

By considering the impact of the field on the absorption cross-section (as per equation 2), we computed the distribution of the field enhancement (E/E0) in both the semiconductor and metallic phases of the VO2 core (as depicted in Figure 3), where |E| and |E0| denote the amplitudes of the total and incident electric fields, respectively.

As indicated in Figures 3a and 3b, the field enhancement at 736 nm was found to be 1.97 in the semiconductor phase and 5.46 in the metallic phase, respectively. At 866 nm, the field enhancement was 5.12 in the semiconductor phase and 5.22 in the metallic phase (as shown in Figs. 3c and 3d). The scattering cross-section (as per equation 3) was plotted to explain the reason for the sharp increase in the field at 736 nm and its smaller increase at 866 nm after the phase change. As shown in Figure 4, the scattering cross-section at 736 nm increases after the phase change. Therefore, at this wavelength, the field increases after the phase change. On the other hand, the scattering cross-section at 866 nm is the maximum in the semiconductor phase. This means that after the phase change, the field does not undergo significant changes.

(a) λ=736 nm (Semiconductor phase) (b) λ=736nm (Metallic phase)

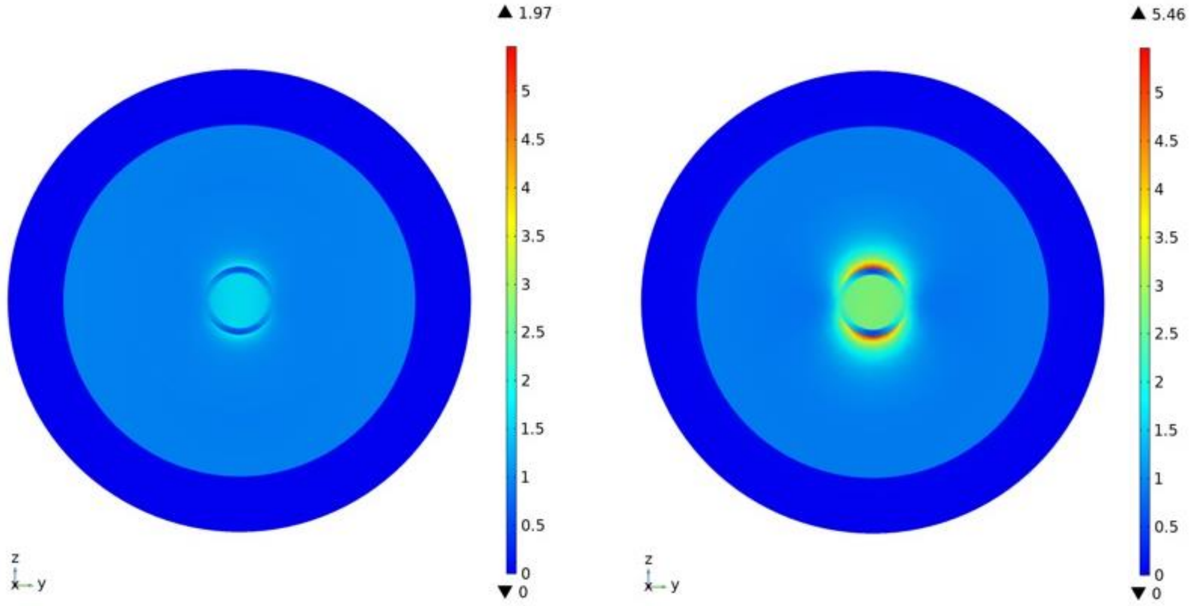

(c) λ=866 nm (Semiconductor phase) (d) λ=866 nm(Metallic phase)

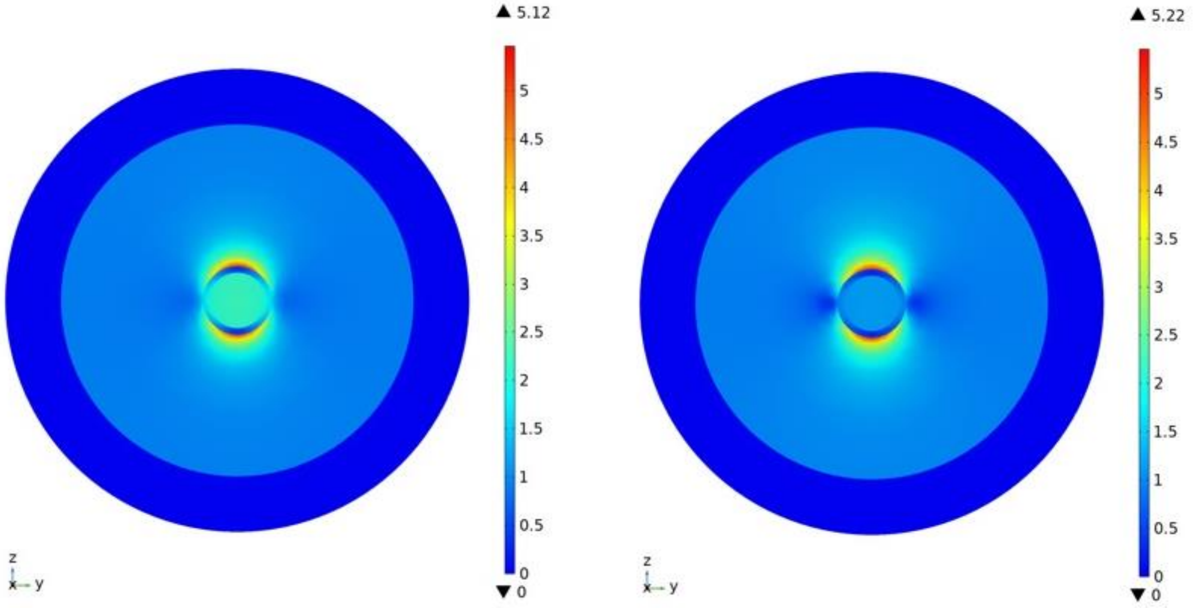

Fig. **3** Illustrates the enhancement of the electric field (E/E_0) in the VO_2@Au nanoshell at 736 nm in both the semiconductor (a) and metallic (b) phases, and 866 nm in the semiconductor (c) and metallic (d) phases of the VO_2 core.

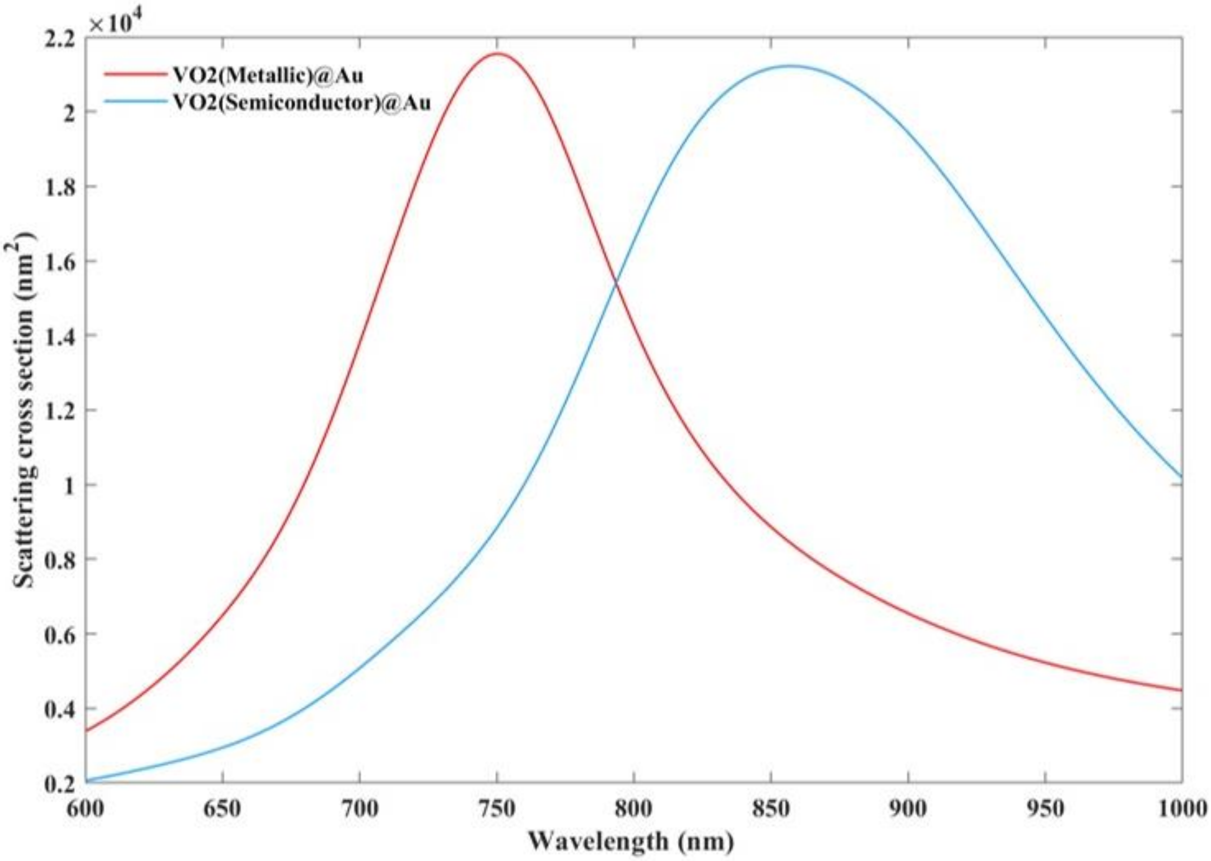

Fig. **4** displays a comparison of the scattering cross-section for a 30@37 nm core-shell in two different phases of the VO_2 core.

B. *Heat Transfer*

To prevent a physical phase transition of the nanoshell and the surrounding medium (i.e., from solid to liquid), we optimized the fluence of the incident laser while the VO2 core underwent a phase transition that could result in a change from a semiconductor to a metal.

The VO2 temperature profile was investigated to identify the laser fluence required for the VO2 interface temperature to increase from the initial ambient temperature of 20°C to the phase transition temperature of 68°C. Fluence thresholds of 2.42 and 1.22 mJ/cm2 were optimized for 736 and 866 nm wavelengths, respectively, for the VO2 core phase transition. At fluences of 3. 055 and 1.643 mJ/cm2 for 736 and 866 nm wavelengths, respectively, VO2 was fully converted to its metallic phase.

Figure 5a illustrates the thermal evolution profile of VO2@Au under pulsed 5 ns laser irradiation with fluences of 2.42 and 3.055 mJ/cm2 at 736 nm. At a fluence threshold of 2.42 mJ/cm2, the delay between peak laser intensity and peak temperature was 1.3 ns (indicated by the blue line). At a fluence of 3.055 mJ/cm2, the delay at the top of the temperature profile was 1.8 ns (indicated by the red line). A delay of 5 ns was observed before (blue line) and after (red line) the phase change at 658 and 736 nm. This delay can be attributed to the increased absorption cross-section following the phase transition of the VO2 core.

As per Figure 5b, a delay of 1.3 ns (blue line) and 1 ns (red line) was observed between the peak of laser intensity and temperature at fluences of 1.22 and 1.643 mJ/cm2, respectively. By comparing the temperature frames for fluences of 1.22 and 1.643 mJ/cm2, it can be seen that the temperature peak of the VO2 core occurs more quickly after the phase transition, which can be attributed to the increase in the absorption cross-section of the semiconductor phase.

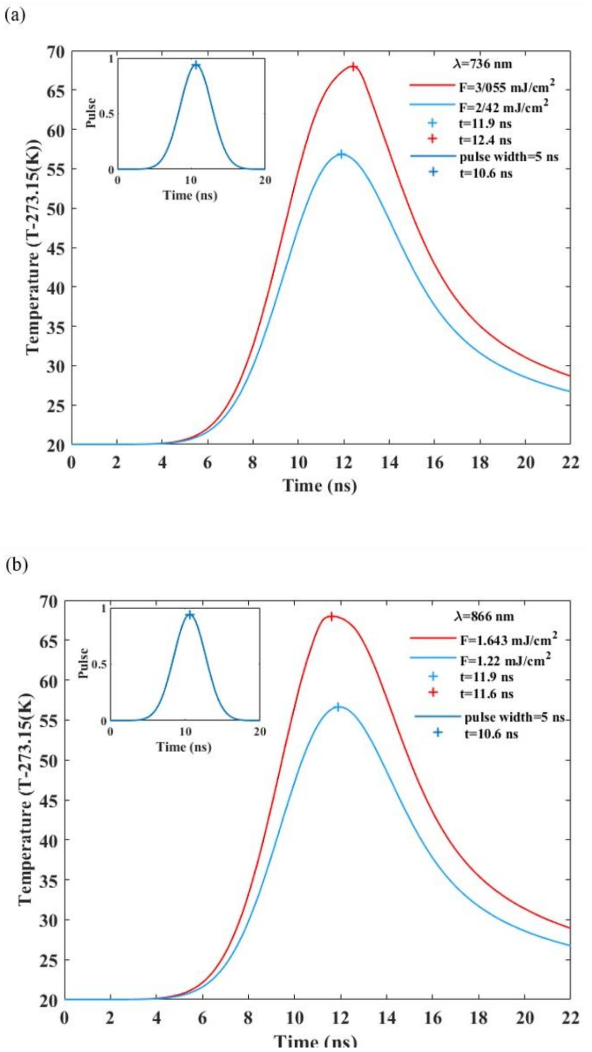

Fig. **5** illustrates the temperature profile on the surface of a 60 nm diameter VO_2 core at (a) 736 nm and (b) 866 nm.

The thermal power density was computed to analyze the contrast between the fluences of 3.055 and 1.643 mJ/cm^2 for inducing a phase transition in the VO_2 core.

Figure 6 illustrates the thermal power density of VO_2, which displays two partially overlapping peaks at a fluence of 3.055 mJ/cm^2 and one at 1.643 mJ/cm^2, corresponding to the phase transition of VO_2. This figure shows that the phase change occurs more quickly at a fluence of 1.643 mJ/cm^2 compared to a fluence of 3.055 mJ/cm^2.

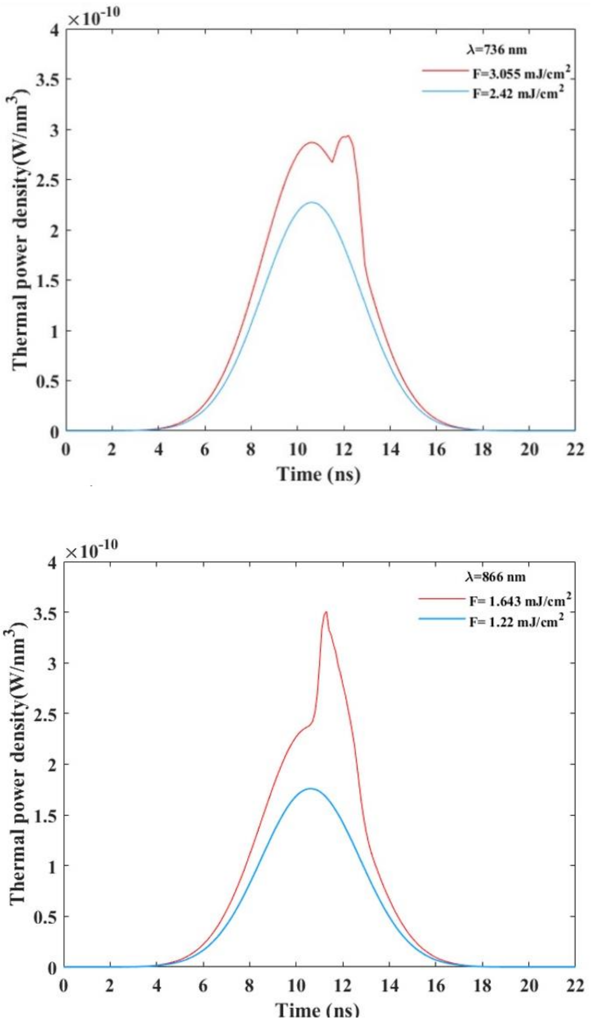

Fig. **6** depicts the thermal power density profile on a 60 nm diameter VO_2 surface at 736 nm (with fluences of 2.42 and 3.055 mJ/cm^2) and 866 nm (with fluences of 1.643 and 1.22 mJ/cm^2).

Figure 7 was used to further investigate the temperature profiles of VO_2@Au and the surrounding environment during and after the laser pulse. This figure shows the temperature rise as a function of distance from the center of VO_2@Au at different times. It can be observed from this figure that, following the laser pulse, as the temperature increases and until the laser pulse reaches its maximum intensity, the temperature inside the NP core rises higher than the temperature of the NP surface. This can be attributed to the phase change and the ability of VO_2@Au to generate and retain more heat in the metallic phase, which has lower thermal conductivity than gold.

When the VO_2 phase changes, the core and shell become isothermal and energy absorption by the core-shell is reduced. Furthermore, as the particle begins to cool after the maximum intensity of the pulse, thermal energy is transferred from the core to the shell and the surrounding medium. Once the laser pulse ceases, heat transfer from the particle to the surrounding medium becomes crucial since there is no longer an energy source in the system. As depicted in the figure, the temperature distribution in the surrounding environment becomes steeper after the phase transition and the heat transferred to the surrounding environment is lower (indicated by the blue line).

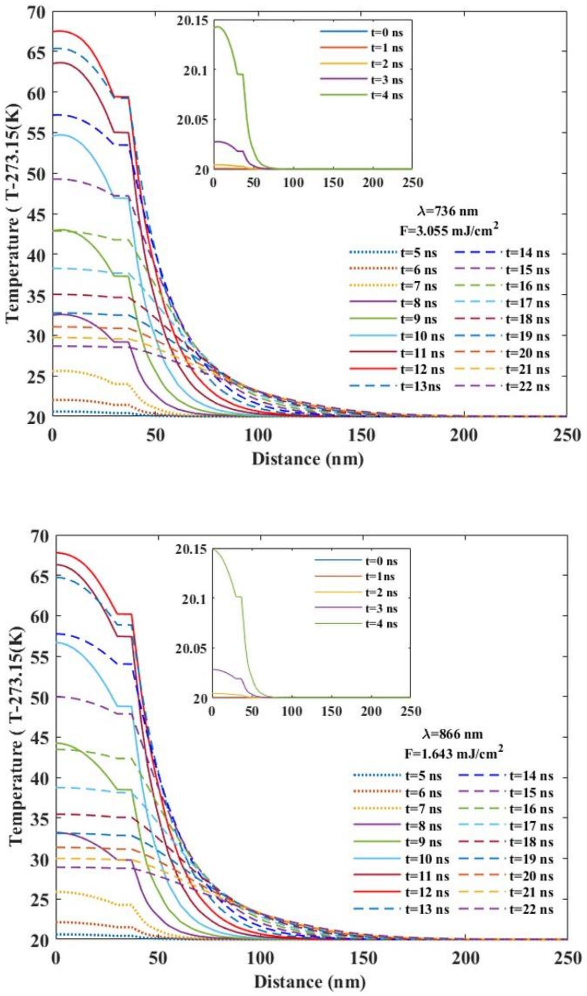

Fig. 7 displays the temperature profile with changes in core-shell distance and environment at (a) 736 nm wavelength and 3.055 mJ/cm^2 fluence, and (b) 866 nm wavelength and 1.643 mJ/cm^2 fluence.

IV. CONCLUSION

In this study, we developed a numerical model to investigate the photonics and thermodynamics of a tunable VO2@Au nanoshell irradiated with a nanosecond pulsed laser. The tunability of the nanoshell is achieved through a photothermal induction process that changes the optical phase of the VO2 core from a semiconductor phase to a metallic phase. We optimized the geometric variables of the nanoshell to maximize the differentiation of the absorption cross-section between the two phases of the VO2 core for photonics. We found that the maximum differentiation occurs at two wavelengths of 736 and 866 nm for a 30 @ 37 nm nanoshell and performed the calculations for these two wavelengths and the fixed size of the nanoshell.

Since the electric field is the primary parameter in calculating the absorption cross-section, we investigated the field distribution inside and outside the nanoshell for the two core phases of VO2. The results showed a significant increase in the field at 736 nm after the phase change, while there was no significant increase at 866 nm. The reason for this behavior was confirmed by scattering cross-section calculations. Since our focus was on the induced photothermal process for the phase change of the VO2 core, we calculated temperature profiles for the optimal fluences required by the pulsed laser.

The laser beams were optimized in such a way that the VO2 core undergoes an optical phase change without any physical phase change (solid to liquid). Upon examining the temperature characteristics for the two optimal incident pulsed laser fluences, we observed a delay in reaching the maximum temperature concerning the maximum incident pulsed laser intensity.

The main objective of this study was to investigate the optical response of the nanoshell when the VO2 core undergoes a structural phase transition. By tuning the optical response of the proposed VO2@Au nanoshell, it can be employed as a smart nano absorber for phototherapy and as a thermal controller.

REFERENCES

[1] Y. Liu, P. Bhattarai, Z. Dai, and X. Chen, “Photothermal therapy and photoacoustic imaging via nanotheranostics in fighting cancer”, Chem. Soc. Rev. vol. 48, pp. 2053–2108, 2019.

[2] J. Ferlay, M. Colombet, I. Soerjomataram, C. Mathers, D. M. Parkin, M. Piñeros, A. Znaor, and F. Bray, “Estimating the global cancer incidence and mortality in 2018: GLOBOCAN sources and methods”, Int. J. cancer, vol. 144, pp. 1941–1953, 2019.

[3] B. Farran B. Farran, R. C. Montenegro, P. Kasa, E. Pavitra, Y. S. Huh, Y. K. Han, M. Amjad Kamal, G. Purnachandra Nagaraju, and G. S. R. Raju, “Folate-conjugated nanovehicles: Strategies for cancer therapy”, Mater. Sci. Eng. C, vol. 107, pp. 110341, 2020.

[4] S.-X. Chen, M. Ma, F. Xue, Sh. Shen, Q. Chen, Y. Kuang, K. Liang, X. Wang, and H. Chen, “Construction of microneedle-assisted co-delivery platform and its combining photodynamic/immunotherapy”, J. Control. Release, vol. 324, pp. 218–227, 2020.

[5] H. Wang, M.R. Revia, K. Wang, M.R.J. Kant, Q. Mu, Z. Gai, K. Hong, and M. Zhang, “Paramagnetic properties of metal-free boron-doped graphene quantum dots and their application for safe magnetic resonance imaging”, Adv. Mater. vol. 29, 2017.

[6] H. K. Moon, S. H. Lee, and H. C. Choi, “In vivo near-infrared mediated tumor destruction by photothermal effect of carbon nanotubes”, ACS Nano, vol. 3, pp. 3707–3713, 2009.

[7] Y. Liu, B. M. Crawford, and T. Vo-Dinh, “Gold nanoparticles-mediated photothermal therapy and immunotherapy”, Immunotherapy, vol. 10, pp. 1175–1188, 2018.

[8] J.-W. Kim, E. I. Galanzha, E. V Shashkov, H.-M. Moon, and V. P. Zharov, “Golden carbon nanotubes as multimodal photoacoustic and photothermal high-contrast molecular agents”, Nat. Nanotechnol. vol. 4, no. 10, pp. 688–694, 2009.

[9] J. Li , H. Xiao, S.J. Yoon, C. Liu, D. Matsuura, W. Tai, L. Song, M. O'Donnell, D. Cheng, and X. Gao, “Functional Photoacoustic Imaging of Gastric Acid Secretion Using pH-Responsive Polyaniline Nanoprobes”, Small, vol. 12, pp. 4690–4696, 2016.

[10] T. Xu , Y. Ma, Q .Yuan, H. Hu, X. Hu, Z. Qian, J.K. Rolle, Y. Gu, and S. Li, “Enhanced ferroptosis by oxygen-boosted phototherapy based on a 2-in-1 nanoplatform of ferrous hemoglobin for tumor synergistic therapy”, ACS Nano, vol. 14, pp. 3414–3425, 2020.

[11] X. Huang, I. H. El-Sayed, W. Qian, and M. A. El-Sayed, “Cancer cell imaging and photothermal therapy in the near-infrared region by using gold nanorods”, J. Am. Chem. Soc. vol. 128, pp. 2115–2120, 2006.

[12] I. V Meglinski and S. J. Matcher, “Quantitative assessment of skin layers absorption and skin reflectance spectra simulation in the visible and near-infrared spectral regions”, Physiol. Meas. vol. 23, pp. 741-753, 2002.

[13] J. Zhou et al., “NIR photothermal therapy using polyaniline nanoparticles”, Biomaterials, vol. 34, pp. 9584–9592, 2013.

[14] B. Khlebtsov, V. Zharov, A. Melnikov, V. Tuchin, and N. Khlebtsov, “Optical amplification of photothermal therapy with gold nanoparticles and nanoclusters”, Nanotechnology, vol. 17, pp. 5167-5179, 2006.

[15] S. Hwang, J. Nam, S. Jung, J. Song, H. Doh, and S. Kim, “Gold nanoparticle-mediated photothermal therapy: current status and future perspective”, Nanomedicine, vol. 9, pp. 2003–2022, 2014.

[16] Y. Ren, Q. Chen, H. Li, H. Qi, and Y. Yan, “Passive control of temperature distribution in cancerous tissue during photothermal therapy using optical phase change nanomaterials”, Int. J. Therm. Sci. vol. 161, pp. 106754, 2021.

[17] A. H. Wyllie, “Cell death,” Cytol. Cell. Physiol. pp. 755–785. 1987.

[18] M. C. Hawes and H. Wheeler, “Factors affecting victorin-induced root cap cell death: Temperature and plasmolysist”, Physiol. Plant Pathol. vol. 20, pp. 137–144, 1982.

[19] P. Purohit, A. Samadi, P. M. Bendix, and J. J. Laserna, “Optical trapping reveals differences in dielectric and optical properties of copper nanoparticles compared to their oxides and ferrites”, Sci. Rep. pp. 1–10, 2020.

[20] P. B. Johnson and R. W. Christy, “Optical Constant of the Nobel Metals”, Phys. Rev. B, vol. 6, pp. 4370–4379, 1972.

[21] A. Hatef, N. Zamani, and W. Johnston, “Coherent control of optical absorption and the energy transfer pathway of an infrared quantum dot hybridized with a VO2 nanoparticle”, J. Phys. Condens. Matter, vol. 29, pp. 155305 (1-9), 2017.

[22] A. Hatef, B. Darvish, A. Dagallier, Y.R .Davletshin, W. Johnston, J. C. Kumaradas, D. Rioux, and M. Meunier, “Analysis of photoacoustic response from gold-silver alloy nanoparticles irradiated by short pulsed laser in water”, J. Phys. Chem. C, vol. 119, pp. 24075–24080, 2015.

[23] Y. Fan, Y. Liu, K. Zhang, Q. Feng, and H. San, “Phase-change regulation criterion based on size-dependent lattice distortion rate and born theory for VO 2 nanomaterials”, Ceram. Int. vol. 47, pp. 3232-3237, 2021.

[24] T. Moradi and A. Hatef, “Thermal tracing of a highly reconfigurable and wideband infrared heat sensor based on vanadium dioxide”, J. Appl. Phys. vol. 127, pp. 24310 (1-10), 2020.

[25] T. Kawakubo and T. Nakagawa, “Phase transition in VO2”, J. Phys. Soc. Japan, vol. 19, pp. 517–519, 1964.

[26] P. Giannios, K. G. Toutouzas, M. Matiatou, K. Stasinos, M. M. Konstadoulakis, G. C. Zografos and K. Moutzouris, “Visible to near-infrared refractive properties of freshly-excised human-liver tissues: Marking hepatic malignancies”, Sci. Rep. vol. 6, pp. 1–10, 2016.

[27] M. Selmi, A. Bajahzar, and H. Belmabrouk, “Effects of target temperature on thermal damage during temperature-controlled MWA of liver tumor”, Case Stud. Therm. Eng. vol. 31, pp. 101821, 2022.

[28] C. Loo *et al.*, ‘Nanoshell-Enabled Photonics-Based Imaging and Therapy of Cancer’, *Technol. Cancer Res. Treat.*, vol. 3, no. 1, pp. 33–40, 2004, doi: 10.1177/153303460400300104.

[29] J. Zhu, R. Huang, M. Ji, G. Su, P. Zhan, and Z. Lu, “Synthesis of monodispersed VO2@Au core-semishell submicroparticles and their switchable optical properties”, J. Mater. Chem. C, vol. 9, pp. 11669–11673, 2021.

[30] I. Balin, S. Wang, P. Wang, Y. Long, and I. Abdulhalim, “Enhanced Transition-Temperature Reduction in a Half-Sphere Au/VO 2 Core-Shell Structure: Local Plasmonics versus Induced Stress and Percolation Effects”, Phys. Rev. Appl. vol. 11, pp. 34064, 2019.

[31] V. T. C. Tsang, X. Li, and T. T. W. Wong, “A review of endogenous and exogenous contrast agents used in photoacoustic tomography with different sensing configurations”, Sensors (Switzerland), vol. 20, pp. 1–20, 2020.

[32] J. Cao, B. Zhu, K. Zheng, S. He, L. Meng, J. Song, and H. Yang, “Recent Progress in NIR-II Contrast Agent for Biological Imaging”, Front. Bioeng. Biotechnol. vol. 7, pp. 1–21, 2020.

[33] Y. Ke, S. Wang, G. Liu, M. Li, T. J. White, and Y. Long, “Vanadium Dioxide: The Multistimuli Responsive Material and Its Applications”, Small, vol. 14, pp. 1–29, 2018.

THIS PAGE IS INTENTIONALLY LEFT BLANK.